Quantitative Mineral Mapping of Drill Core Surfaces II:
Long-Wave Infrared Mineral Characterization Using *μ*XRF and Machine Learning

Rocky D. Barker,[1,†] Shaun L.L. Barker,[2] Matthew J. Cracknell,[2] Elizabeth D. Stock,[3] and Geoffrey Holmes[1]

[1]School of Science, University of Waikato, Private Bag 3105, Hamilton, New Zealand 3240

[2]CODES ARC Centre of Excellence in Ore Deposits, University of Tasmania, Private Bag 126, Hobart, Tasmania, Australia 7001

[3]Barrick Gold Exploration Inc., 1655 Mountain City Hwy, Elko, Nevada 89801

Abstract

Long-wave infrared (LWIR) spectra can be interpreted using a Random Forest machine learning approach to predict mineral species and abundances. In this study, hydrothermally altered carbonate rock core samples from the Fourmile Carlin-type Au discovery, Nevada, were analyzed by LWIR and micro-X-ray fluorescence (*μ*XRF). Linear programming-derived mineral abundances from quantified *μ*XRF data were used as training data to construct a series of Random Forest regression models. The LWIR Random Forest models produced mineral proportion estimates with root mean square errors of 1.17 to 6.75% (model predictions) and 1.06 to 6.19% (compared to quantitative X-ray diffraction data) for calcite, dolomite, kaolinite, white mica, phlogopite, K-feldspar, and quartz. These results are comparable to the error of proportion estimates from linear spectral deconvolution (±7–15%), a commonly used spectral unmixing technique. Having a mineralogical and chemical training data set makes it possible to identify and quantify mineralogy and provides a more robust and meaningful LWIR spectral interpretation than current methods of utilizing a spectral library or spectral end-member extraction. Using the method presented here, LWIR spectroscopy can be used to overcome the limitations inherent with the use of short-wave infrared (SWIR) in fine-grained, low reflectance rocks. This new approach can be applied to any deposit type, improving the accuracy and speed of infrared data interpretation.

Introduction

Short-wave infrared (SWIR) spectroscopy techniques are increasingly utilized in mining and mineral exploration to recognize and classify various mineral species of significance for exploration and mineral processing (Ahmed, 2010; Browning, 2014; Maydagán et al., 2016; Bedell et al., 2017). Short-wave infrared spectroscopy is commonly used in porphyry (Pour and Hashim, 2015; Han et al., 2018; Neal et al., 2018) and epithermal exploration (Crósta et al., 2003; Hooper et al., 2018). Recent efforts have been made to apply infrared spectroscopy techniques such as handheld and benchtop infrared analyzers (Ahmed, 2010; Bradford, 2008; Ahmed et al., 2009; Mateer, 2010; Browning, 2014), and, most recently, infrared core scanning technologies (Barker, 2017; Barker and Ridley, 2020) to Carlin-type gold deposits in Nevada. The utility of SWIR for Carlin-type gold deposits, however, has been limited due to the low reflectivity of samples which often produces flat, undiagnostic spectra.

In order to overcome the lack of reflectance and the difficulty of distinguishing minerals such as quartz and feldspars in SWIR, LWIR spectroscopy has been implemented by hyperspectral core logging systems such as the Hylogger-3 (Mauger et al., 2012; Arne et al., 2016) and SisuROCK (Tappert et al., 2015). However, many minerals contained within these fine-grained samples have characteristic peaks that overlap within the spectral range used in this study (7,500–12,000 nm, Salisbury, 2020). In addition, the impact of volume scattering in fine-grained rocks (Ramsey and Christensen, 1998; Zaini et al., 2012; Laukamp et al., 2018), grain orientation (McDowell et al., 2009; Tappert et al., 2013), and grain size (Zaini et al., 2012; Laukamp et al., 2018) on LWIR spectra have hampered our ability to interpret LWIR for mineralogy and mineral chemistry. In this contribution, we demonstrate the use of micro-X-ray fluorescence (*μ*XRF) mapping, supported by machine learning, to provide robust, quantitative analysis of LWIR spectra to predict mineral abundances within LWIR-scanned rock samples. Previous attempts at quantifying LWIR spectral mixtures often involved the use of linear spectral mixture analysis (Gillespie, 1992; Ramsey and Christensen, 1998; Feely and Christensen, 1999; Ramsey, 2004), which requires a complete spectral library of all minerals present in the system. A reference library with a disproportionate number of end-member spectra to the mineral system in question can lead to high error and overfitting (Rogge et al., 2006; Hecker et al., 2012).

In this study, *μ*XRF data were matched to LWIR spectra, and machine learning approaches were used to train models to predict minerals present within each LWIR image pixel. This method is similar to that presented in Hecker et al. (2012), where petrographic point counts were used as training data for a partial least-squares regression algorithm. The method for infrared mineral identification presented here circumvents the need to interpret the tremendous possible variations in spectral mixtures and obviates the need for a spectral library to be produced for each individual geologic domain. This approach could be broadly applied to any deposit type, potentially improving the speed and accuracy of spectral data interpretation by removing the need for custom libraries or relying on SWIR and LWIR spectra alone for mineralogical interpretation.

†Corresponding author: email, rdb28@students.waikato.ac.nz

The rock samples in this study are fine-grained, carbonaceous, calcareous, hydrothermally altered sedimentary rocks from the Fourmile Carlin-type gold discovery, Nevada (Fig. 1). Typical samples may contain carbonate minerals, phyllosilicates, feldspars, and quartz, all of which have been shown to have characteristic features in the LWIR spectral range (Nash and Salisbury, 1991; Lane and Christensen, 1997; Yitagesu et al., 2011).

Data and Methods

Sampling

Infrared scanning using the SisuROCK core imaging system provided by the company TerraCore was completed on 2,030 m of HQ drill core from seven drill holes, which passed through hydrothermally altered and unaltered sedimentary carbonate and minor low-grade metamorphic host rocks in a transect across the Fourmile Au discovery (Fig. 1). One hundred core samples ≤30 cm in length were collected from the infrared-scanned drill core for μXRF and whole-rock geochemical analysis. Of the 100 μXRF samples, 12 were used in this study (Table 1). These samples were selected to represent the full range of lithology types and alterations found in the IR-scanned drill core. Mineralogy of the samples selected was determined by XRD analysis of powders taken from the same 12 μXRF analyzed samples selected for this study.

Micro-XRF mineralogy

There are two primary reasons a μXRF chemical rastering technique was selected to inform LWIR spectra. First, the similarity of the rastering techniques between μXRF and infrared imaging produces data that are spatially referenced and can be related to one another using an image registration technique. Second, μXRF provided a way to estimate mineralogy independent of infrared techniques and produces a significant number of sample points (or pixels, ~1 × 10^6 points per μXRF image) for robust statistical analysis. The μXRF geochemical maps were produced on a Bruker Tornado μXRF (Bruker, 2018c), using a 100-μm step size (pixel

size) and 25-μm spot size with standard conditions of analyses at 10 msec per pixel dwell time, two frame counts, and 50-kV acceleration voltage at the AuTec Laboratory in Vancouver, Canada. Quantitative chemical results were derived using the Bruker M4 (Bruker, 2018a) QMap fundamental parameter standardless quantification tool (Flude et al., 2017).

A linear programming algorithm was used to calculate mineralogy from quantified μXRF geochemistry. This method uses mineral formulas obtained through electron microprobe analysis to calculate mineralogy from fundamental parameter quantification of μXRF chemical maps (see Barker, et. al., 2020, for complete method description). Quantification from the fundamental parameter method using Bruker M4 software was completed on a 9- × 9-pixel grid, giving a final resolution of ~ 0.9 mm per pixel (aggregation of eighty-one 100-μm pixels).

Infrared spectroscopy

All hyperspectral scanning was completed using the SisuROCK core imaging system provided by the company TerraCore for VNIR, SWIR, LWIR, and RGB. The RGB camera produces 160-μm spatial resolution visible light images. For this project, the FENIX VNIR (350- to 1,000-nm range, 3.5-nm spectral resolution) and SWIR (1,000- to 2,500-nm range, 12-nm spectral resolution) camera produced coregistered images at 1.2-mm spatial resolution and a total of 410 bands. The OWL LWIR camera provided 1.2-mm spatial resolution images with 96 bands (7,500–12,000 nm) and 100-nm spectral resolution.

Preprocessing of hyperspectral data was completed by TerraCore. TerraCore uses the empirical line calibration method (ELC; Smith and Milton, 1999) for conversion of raw spectral data to reflectance. The ELC method directly compares image data and real spectra by using spectrally uniform light and dark pixels to draw a line-fitting algorithm to convert the raw digital numbers produced from the spectral cameras into physical units of reflectance (Bedell and Coolbaugh, 2009). In the case of TerraCore, the white and dark references are collected for each image during the scanning process. The white and dark references are then used to derive a linear

Table 1. Summary of Image Registration Tie Points Showing Total Number of Points and Root Mean Square Error as a Measure of "Goodness of Fit," as well as the Sample Information for Each of the Core Grab Samples[1]

Sample no.	Points	RMSE	X R^2	Y R^2	Drill hole	Depth [m]	Rock description
M180062	17	3.96	1.000	0.998	FM16-01D	609.57	Silicified and brecciated limey carbonaceous mudstone with illite enrichment
M180069	23	5.35	1.000	0.999	FM16-01D	863.44	Limestone with minor silicification and argillization
M180074	19	8.80	0.999	0.997	FM16-01D	1071.59	Sulfidized and argillized muddy limestone
M180077	19	6.06	1.000	0.997	FM16-07D	706.53	Metacarbonate breccia with silicified clasts
M180080	Visual test sample (not registered)				FM16-07D	823.48	Limey mudstone with silica replacement front
M180083	17	4.96	1.000	0.999	FM16-07D	906.48	Dolomitic metacarbonate
M180088	22	8.27	1.000	0.996	FM16-07D	1118.07	Base metal vein-bearing marl with minor silicification
M180093	18	7.53	0.999	0.984	GRC-0427D	685.69	Metacarbonate with pinstripe pyrite and minor silicification
M180102	8	7.85	0.999	0.928	GRC-0427D	877.00	Muddy limestone with minor silicification and argillization
M180104	18	5.73	1.000	0.990	GRC-0427D	925.07	Mineralized limey mudstone breccia with pervasive silicification and sulfidation
M180118	19	4.11	1.000	0.997	GRC-0436D	765.20	Muddy limestone with minor silicification and argillization
M180121	13	4.42	0.999	0.999	GRC-0432D	200.62	Weathered carbonaceous limey mudstone with minor argillization and silicification

[1]Points refers to the number of tie points selected for each sample; the X and Y R^2 values refer to the R^2 in both the X and Y axes; the drill hole and depth is the ID of the drill hole and depth in which the sample came from (see Fig. 1 for geographic location)
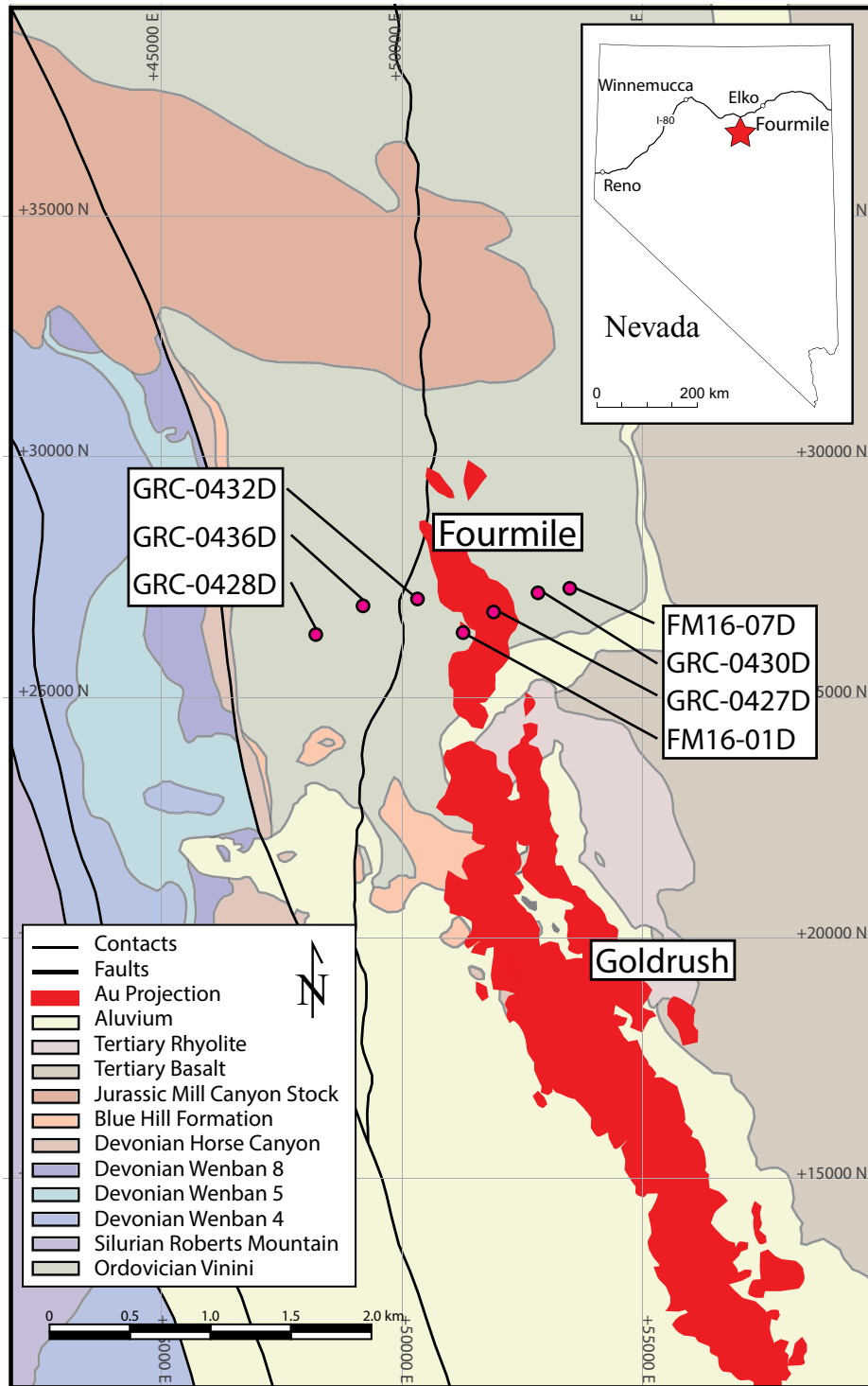
Fig. 1. Regional geologic map of the Goldrush-Fourmile district from Barrick Gold Exploration Inc. unpublished results (2019) with locations of drill holes, which sourced the samples for this study.

adjustment between the raw digital number and the actual reflectance measured from the reference (Bedell and Coolbaugh, 2009). This is done on each box of scanned core to ensure consistent data collection.

For all LWIR data, a continuum removal was applied using the linear interpolation and division normalization method (Clark and Roush, 1984) in the R statistical programming language (R Core Team, 2017).

Image registration

Image registration was completed on 11 of the 12 μXRF images where the μXRF image was registered to a LWIR

image of the same sample. Image registration is the process of aligning two images of the same object to compare images from multiple sources, sensor types, and spatial resolutions. Images from this study were registered by manually selecting tie points of the base and warp images in the R statistical programming language (R Core Team, 2017). The tie points were used to calculate a homography and apply an affine transformation using the R packages "raster 2.8-4" (Hijmans, 2018), and "imager 0.41.1" (Barthelme, 2018). Resampling of pixels, or the creation of new pixels in the warp image, was completed using a nearest neighbor resampling method (Canty, 2014). The final products were evaluated for accuracy by measurement of tie points to a predicted location on the warp image. The predicted location is based on a first-order polynomial transform that is generated from the tie points on the base image. A total root mean square error (RMSE) is produced for each image and is taken as a measurement of the overall fit of the tie points when combined with a visual assessment of overlaid base and warp images (Jin, 2017). Table 1 summarizes the number of tie points and RMSE for each sample.

Random Forest classification and regression

Random Forest is an example of an ensemble algorithm, which is designed to combine multiple weak, independently trained models, in this case decision trees, to make an overall prediction (Breiman, 2001). Decision trees generate classification or regression predictions by constructing a model from available training data (Breiman et al., 1984; Quinlan, 1986). Decisions are made at nodes in the tree structure based on splitting criteria that iteratively pass observations down the tree until a prediction decision is made for the given input. Decision trees can be sensitive to changes in the training sets such that different subsets of data can result in vastly different outcomes. Random Forest attempts to alleviate this problem by taking random subsamples from the training data to construct individual decision trees. The final prediction is based on a majority class vote for classification, or the average value for regression (Brownlee, 2018).

The Random Forest v4.6-14 package (Liaw and Wiener, 2002) was used to construct regression models and assess model performance. For each Random Forest model, the number of trees grown (ntree) was left at the default value of 500. The number of variables randomly sampled as candidates at each split (mtry) was also left at the default values of $\sqrt{p}$ for classification and $p/3$ for regression, where p is the number of variables in the dataset. A series of ntree and mtry values were evaluated using the R package "caret" (v6.0-85; Kuhn, 2020) for each classification and regression model, with a range from 250 to 3,000 for ntree and 1 to 60 for mtry. No significant changes in classification accuracy or regression RMSE were observed across different ntree or mtry values.

A Random Forest binary classification model was used to generate a mask for the LWIR images for the purpose of reducing computational time, limiting false identification of core box pixels, and to improve the aesthetic of false color images. Regions of interest were manually selected from five core-box images and labelled as "rock" or "box." The resulting Random Forest classifier was created with a total of 52,342 samples (12,973 box and 39,369 rock), 36,639 of which were training and 15,703 test samples, and 96 variables (LWIR bands). The resulting mask model produced results with an accuracy (proportion of correctly identified pixels to total number of pixels) of 0.98. The mask model was run on each box image prior to mineral identification. Pixels that resulted in a box label were given a null value.

Random Forest regression models were created by registering μXRF-derived mineralogy raster images to LWIR spectral images as training data for the following minerals: calcite, dolomite, kaolinite, white mica, potassium feldspar, phlogopite, and quartz. The total number of data points for the infrared regression models is shown in Table 2. Each data point contained 102 variables, 96 of which were LWIR band intensities (LWIR spectra) and six were spectral features that were extracted from the LWIR spectra, such as peak and trough wavelength positions and peak intensity ratio (Table 3).

Performance of models was measured by doing a 70/30 train-test split and calculating the root mean square error (RMSE) and R^2 (Pearson), slope, and intercept of the line of best fit (least-squares method) between training test values (mineralogy from μXRF) and predicted values (mineralogy from LWIR). Both RMSE and R^2 are measurements of how well a dataset fits to a line that is produced from the input and predicted values. To verify that the predictions are not over- or underestimated, the slope of the line should be close to one and the intercept should be near zero. Therefore, the slope and intercepts are used in conjunction with RMSE and R^2 for a more complete performance measurement of the model.

External validation

The LWIR-derived mineralogy results were aggregated to multielement geochemistry and assay intervals (5, 10, and

Table 2. Number of Training and Test Samples (pixels) Used for Each Mineral Model

Model	Training samples	Test samples
Calcite	85,911	33,506
Dolomite	57,248	24,535
Kaolinite	28,048	12,021
K-feldspar	28,675	11,296
White mica	54,570	23,388
Phlogopite	8,959	3,840
Quartz	65,713	28,163

Table 3. Summary of LWIR Feature Variables Used in the Random Forest Mineral Regression Models[1]

Feature	Range (nm): from	To (nm)
Maximum	7,717	8,376
Maximum	8,423	9,599
Maximum	7,717	9,599
Maximum	10,916	11,528
Minimum	7,952	8,987
Ratio	~8,000	~9,000

[1]Maximum refers to a spectral "peak" and minimum is a spectral "trough;" the range describes the bands that were evaluated for the feature position; the resulting data is a wavelength value that contains the highest or lowest point for peaks and troughs, and the ratio is the maximum of the ~8,000 nm (7,717–8,376 nm) divided by the maximum of the ~9,000-nm feature (8,423–9,599 nm)

20 ft) for the same 2,030 m of drill core samples. The multielement geochemistry and assay, provided by Barrick Gold Exploration Inc., were analyzed at ALS, Elko, Nevada for Au and Ag assay and 48 element, 4-acid digest geochemistry (Li, Be, Na, Mg, Al, P, S, K, Ca, Sc, Ti, V, Cr, Mn, Fe, Co, Ni, Cu, Zn, Ga, Ge, As, Se, Rb, Sr, Y, Zr, Nb, Mo, Ag, Cd, In, Sn, Sb, Te, Cs, Ba, La, Ce, Hf, Ta, W, Re, Hg, Tl, Pb, Bi, Th, and U). Predicted elemental concentrations (from Random Forest models) were calculated using the mineralogy predictions and compared to multielement geochemistry from each interval for Al, Ca, K, and Mg. Carbon was estimated from multielement geochemistry by calculating CO_2 from carbonate in the following equation:

$$CO_2 = \frac{MgO}{CO_{2Dol}} + \left[CaO - \frac{MgO}{CaO_{Dol}} \right] \left[\frac{1}{CO_{2Cal}} \right],$$

where CO_{2Dol} is the proportion of CO_2 in dolomite (0.458), CaO_{Dol} is the proportion of CaO in dolomite (0.719), and CO_{2Cal} is the proportion of CO_2 in calcite (1.274). This method cannot account for organic C and so there must be an assumption that organic C is minor compared to C from carbonate. This assumption is considered to be reasonable because of the low organic content of samples from the unaltered Roberts Mountain Formation (~0.25%; Wells and Mullens, 1973; Clark Maroun et al., 2017) and the altered and unaltered Wenban Formation (<0.05–0.25%; Wells et al., 1969) of the neighboring Cortez Hills Au district. Silica for four acid ICPMS analyses (which do not provide Si concentrations) was calculated by summing all oxides, including the calculated carbonate in the equation:

$$SiO_2 = 100 - \Sigma(Measured\ Oxide + CO_2),$$

which assumes that the missing chemical component is SiO_2. This approach for estimating C and Si was validated by comparing the predicted results to those obtained from the 100 whole-rock geochemical laboratory analyses. Samples used to verify the Si and C calculation method were characterized for whole-rock geochemistry by ALS Laboratory in Reno, Nevada, using a "complete whole rock characterization package," which includes major elements measured by XRF and ICP-AES on lithium borate fused disks, trace elements by ICPMS on fused beads, and total carbon and sulfur measured by infrared combustion (LECO) analysis.

Results

Long-wave infrared (LWIR) was chosen for this study due to the lack of reflectivity of the Carlin-type gold deposit host rocks in the short-wave infrared (SWIR) range. Figure 2 is an example of the Carlin-type gold deposit rocks used in this study with a comparison of the SWIR and LWIR spectra from five points taken throughout the box of core. It shows that SWIR spectra from these points are flat and undiagnostic, whereas the LWIR spectra has characteristic peaks that can be used for mineral identification. A scatter plot of peak intensity relative to measured albedo for SWIR and long-wave infrared (LWIR) data (Fig. 3) shows the lack of SWIR response in low albedo samples compared to that of LWIR, which demonstrates the limitation of SWIR in dark lithologies. In addition, a plot of the same samples illustrating the intensity of carbonate peaks in the LWIR range correlates to variations in Ca content derived from multielement geochemistry, whereas there is no obvious association in the SWIR due to the lack of reflectance (Fig. 4).

LWIR spectra

Sample LWIR spectra from individual pixels show multiple spectral absorption features indicating a mixture of mineralogy (Fig. 5). In most cases, the spectra from each pixel likely contains more than just the target mineral, due to the fine-grained nature of the rocks, causing characteristic peak overlap and volume scattering (Ramsey and Christensen, 1998), which makes spectral library matching for quantification difficult (Fig. 5).

LWIR Random Forest regression models: predicted mineral proportions

Random Forest regression models for mineral identification were constructed using LWIR spectra of LWIR raster images trained by μXRF-derived quantitative mineralogy. Samples (pixels) were split in a 70/30 ratio where 70% was used to train the models and 30% used to test the predictions of the models. The RMSE for model predictions (measured versus predicted) ranged between 1.17 and 6.75%, with R^2 values of 0.82 to 0.94, and regression lines with slopes near one (1.01-1.09) and intercepts near zero (–0.70 - –0.09) for calcite, dolomite, white mica, kaolinite, K-feldspar, phlogopite, and quartz (Fig. 6).

A test μXRF sample was withheld from model training for the purpose of validation of the textural and geologic significance of the Random Forest results. Figures 7 and 8 show side-by-side comparisons of μXRF-derived quantified mineralogy and LWIR Random Forest quantified mineralogy results for sample M180080 for the minerals calcite, dolomite, quartz, and white mica. For descriptive purposes, sections of the sample are numbered in Figures 7 and 8 according to textural significance where (1) is the relatively unaltered host rock, (2) is the larger calcite + quartz veins in the unaltered host rock, (3) shows the silicification front, (4) is the zone of pervasive silicification, (5) shows a thin dolomite vein, and (6) is a zone of high calcite in the lower right corner of the image.

Large calcite veins can be identified in the LWIR Random Forest results (2), as well as calcite in the host rock (1), along the silicification front (3), and in the lower right corner of the image (6). Calcite veins seen in the μXRF image, which are smaller than the spatial resolution of the LWIR image, cannot be clearly recognized in the LWIR image. Some variation in calcite quantity is predicted in the host rock (1) that is not apparent in the μXRF image. It appears the Random Forest model predicted the left side of the image to be slightly higher in calcite abundance than the right (Fig. 7A, B).

Dolomite (Fig. 7C, D) in the predicted LWIR image has similar general textures in the host rock (1) as in the μXRF. Much of the textural detail is lost in the LWIR image, such as the small grains of dolomite that can be seen in the μXRF, but the general presence of dolomite in the host rock (1) and not in the silicified section (3, 4) nor the calcite + quartz vein (2) are similar. Many of the small dolomite veins (5), which are thinner than the spatial resolution of the LWIR, are also not visible in the LWIR image. There also appears to be a small

Fig. 2. Example spectrum from a typical box of core from hole FM16-07D, 801.6-804.2-m depth. The color dots in the true-color image (top) show the location of the extracted VN-SWIR (middle) and LWIR (bottom) spectra. This figure shows the difficulty in interpreting VNIR-SWIR spectrum from Carlin-type spectrum and why LWIR may be the preferred spectral range.
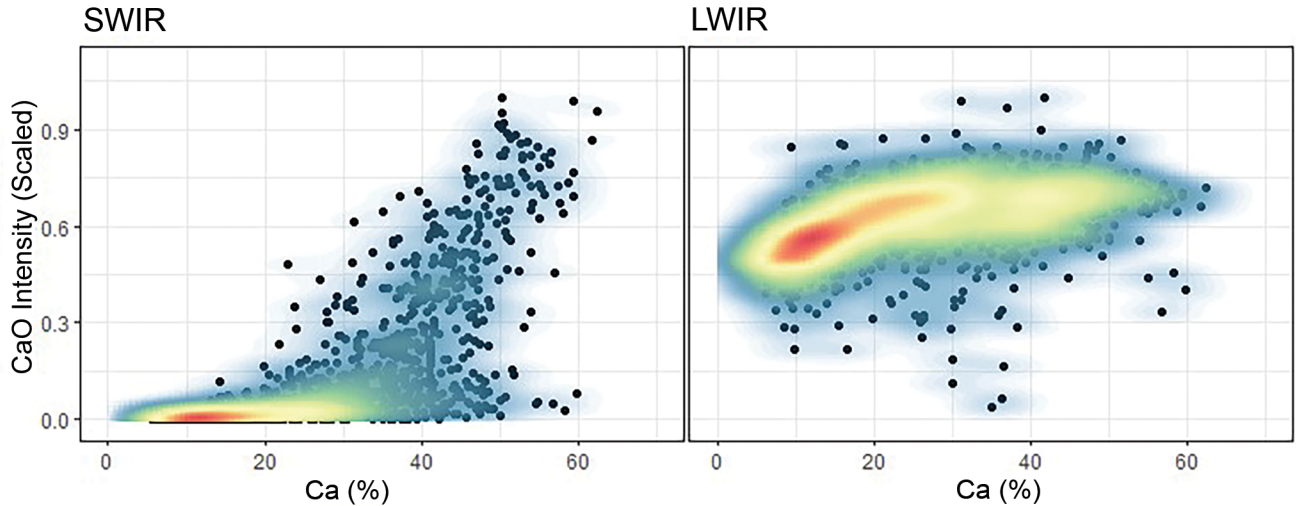
SWIR   LWIR

Fig. 3. Results of infrared-scanned drill core from seven drill holes (FENIX and OWL sisuRock core imaging systems) at ~10-ft composites (image pixel results aggregated to the assay intervals) for a total of 1,531 samples. SWIR CaO intensity (~2,340-nm feature) and LWIR CaO intensity (~11,200-nm feature) compared to sample albedo measurements (total reflectance of sample in VNIR compared to white and dark reference). SWIR response minimal up to ~20 to 30% albedo, whereas LWIR response shows little change related to albedo.

amount of calcite predicted as dolomite in the lower portion of Figure 6.

The quartz mineral maps (Fig. 8A, B) are of similar abundances and show most of the same textures such as a quartz vein (2), silicification front (3), pervasive silicification (1), and lack of silicification (6) in the carbonate-rich zones. Like calcite, there appears to be variation in the quartz quantity within the host rock (1) of the LWIR image that is not seen in the μXRF, except the increase in quantity is seen on the right side.

The white mica mineral maps (Fig. 8C, D) have very similar quantities between the LWIR and μXRF. General textures between the two images appear to agree in the region of the silicification front (3), pervasive silicified zone (4), and calcite zone (6). There appears to be some error in the prediction of the host-rock composition (1). The μXRF shows variable white mica from ~5 to 15% with the highest quantities around the larger calcite + quartz veins. The Random Forest has predicted the host rock to have a more homogeneous white mica distribution (possibly because of the coarse resolution of the
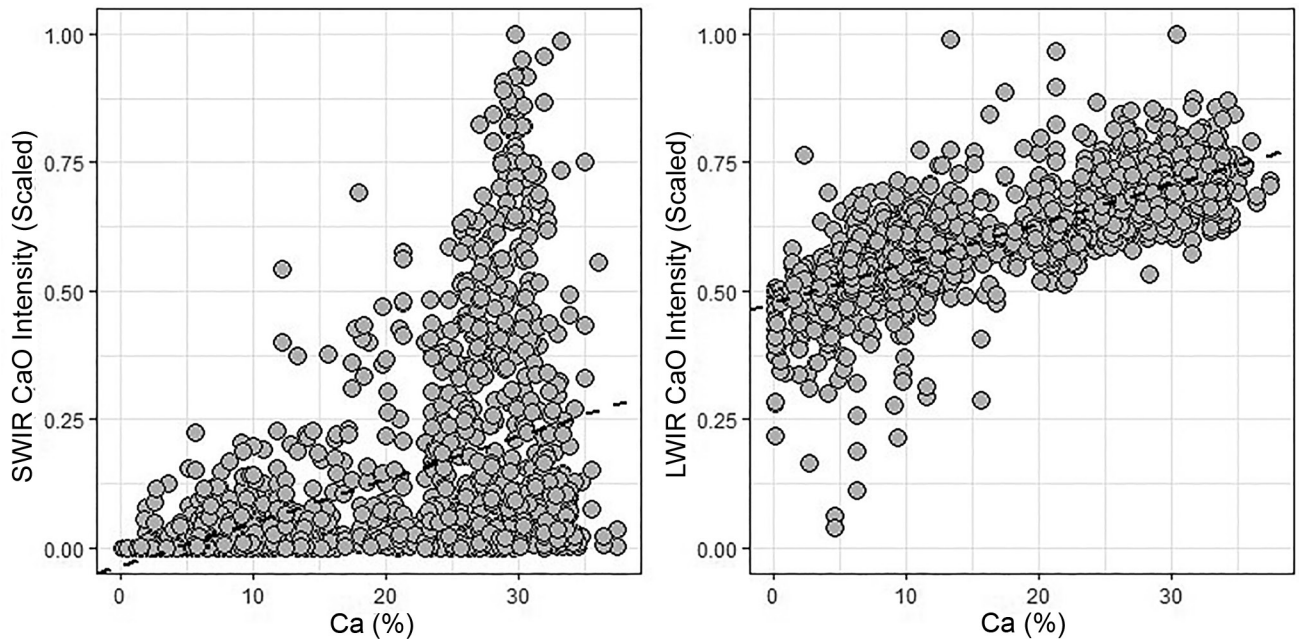

Fig. 4. Results of infrared-scanned drill core from seven drill holes at ~10-ft composites (image pixel results aggregated to the assay intervals) for a total of 1,531 samples (same samples from Fig. 3). Intensity of SWIR (~2,340 nm) and LWIR (~11,200 nm) CaO features compared to Ca from 4-acid digest multielement geochemistry of the same intervals. Clear linear relationship can be seen in LWIR, which is not present in SWIR.
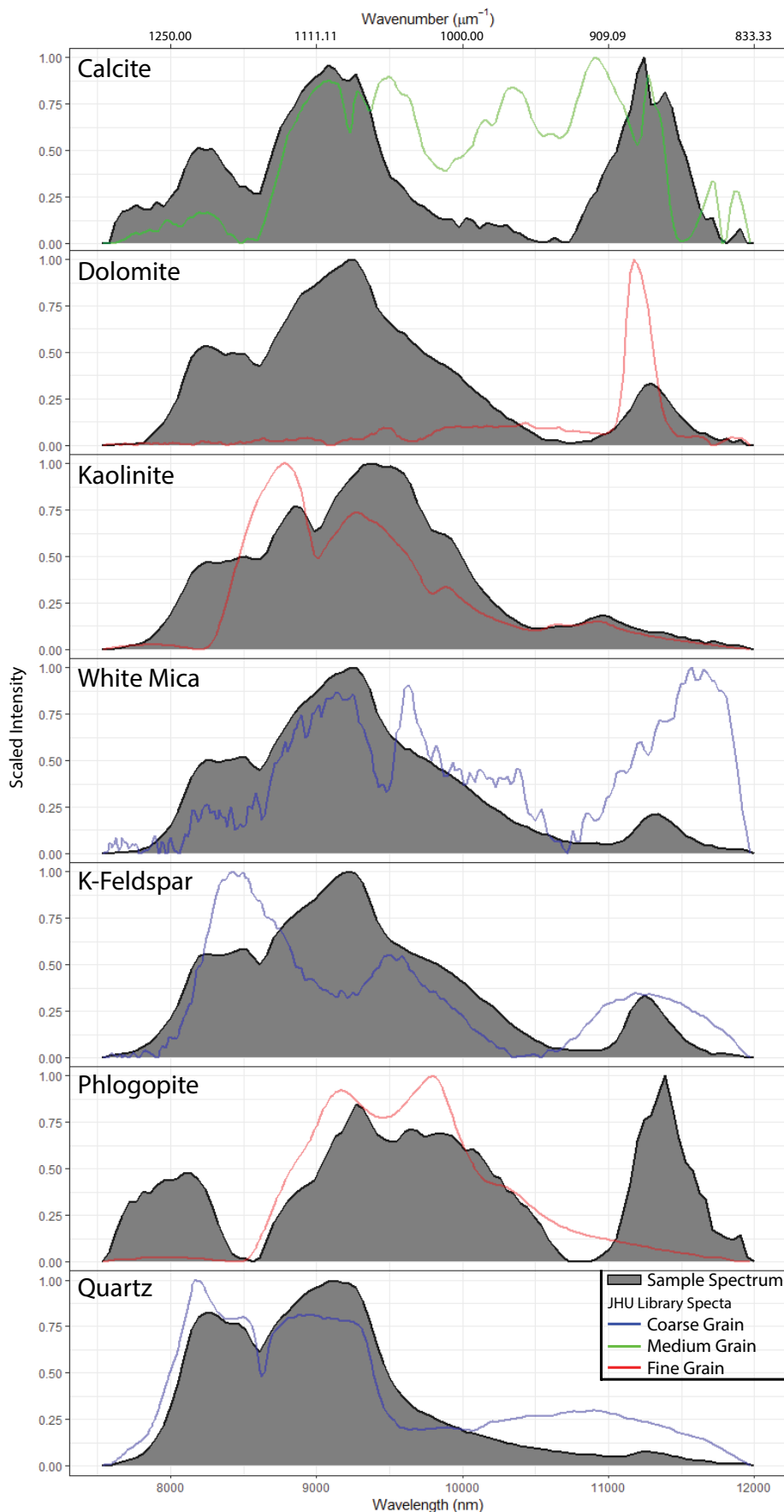
Fig. 5.   LWIR spectra (gray) from selected samples of known mineral species (known from QXRD; see Barker, et. al., 2020, for QXRD methods) to show spectral response. Library spectra (red, green, and blue lines) from the John Hopkins University spectral library (Salisbury, 2020) are overlaid for a comparison. Blue spectral lines indicate spectra from a coarse-grained mineral sample, green from medium-grained, and red from fine-grained.
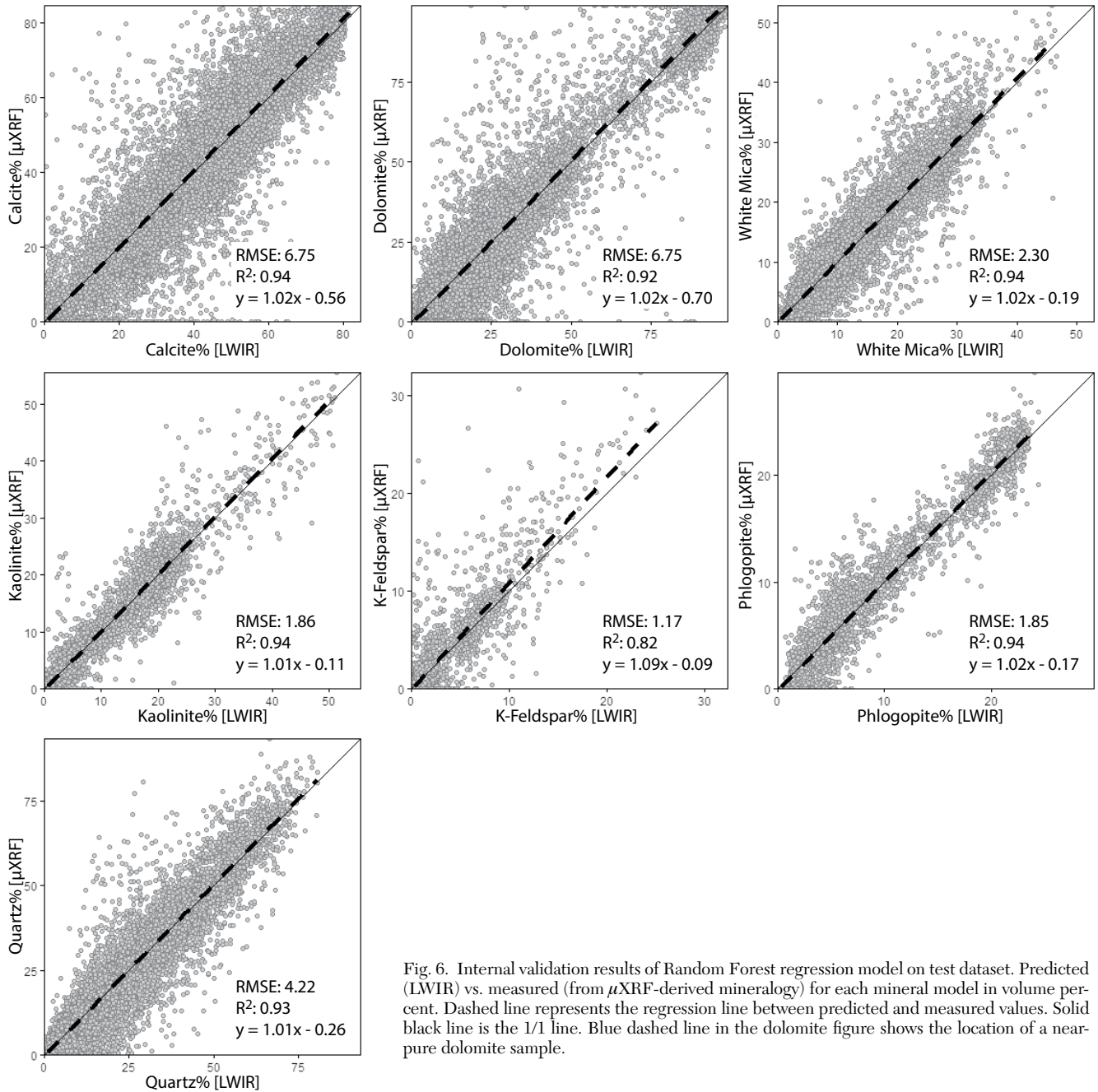
Fig. 6. Internal validation results of Random Forest regression model on test dataset. Predicted (LWIR) vs. measured (from μXRF-derived mineralogy) for each mineral model in volume percent. Dashed line represents the regression line between predicted and measured values. Solid black line is the 1/1 line. Blue dashed line in the dolomite figure shows the location of a near-pure dolomite sample.

LWIR images) and to be generally higher in abundance, with slightly less mica around the calcite + quartz veins.

Visually, the predicted mineralogy results have similar textures and mineralogical patterns as that of the μXRF-derived mineralogy map of the test sample for calcite, dolomite, quartz, and white mica (Figs. 7, 8). However, minor differences can be seen in some of the mineral distributions, especially when it comes to loss of detail (due to the change in image resolution between XRF and LWIR).

Variable importance

The variable importance is a measure of how much a variable increases accuracy when included or decreases accuracy when omitted. It is a typical method for understanding and interpreting the inner workings of a Random Forest model as it provides a record of the variables which are most diagnostic for a prediction. Figure 9 shows the variable importance displayed as a function of wavelength and thus shows which wavelengths were most important in the creation of each mineral model. In some cases, such as dolomite and quartz, characteristic features were the primary variables used in creating the models. Other models like kaolinite however gained the most accuracy by utilizing peak wavelengths such as the ~8,000- to 9,000-nm feature position, as well as some other LWIR bands that don't appear to be related to recognized spectral features present on reference spectra. In these other
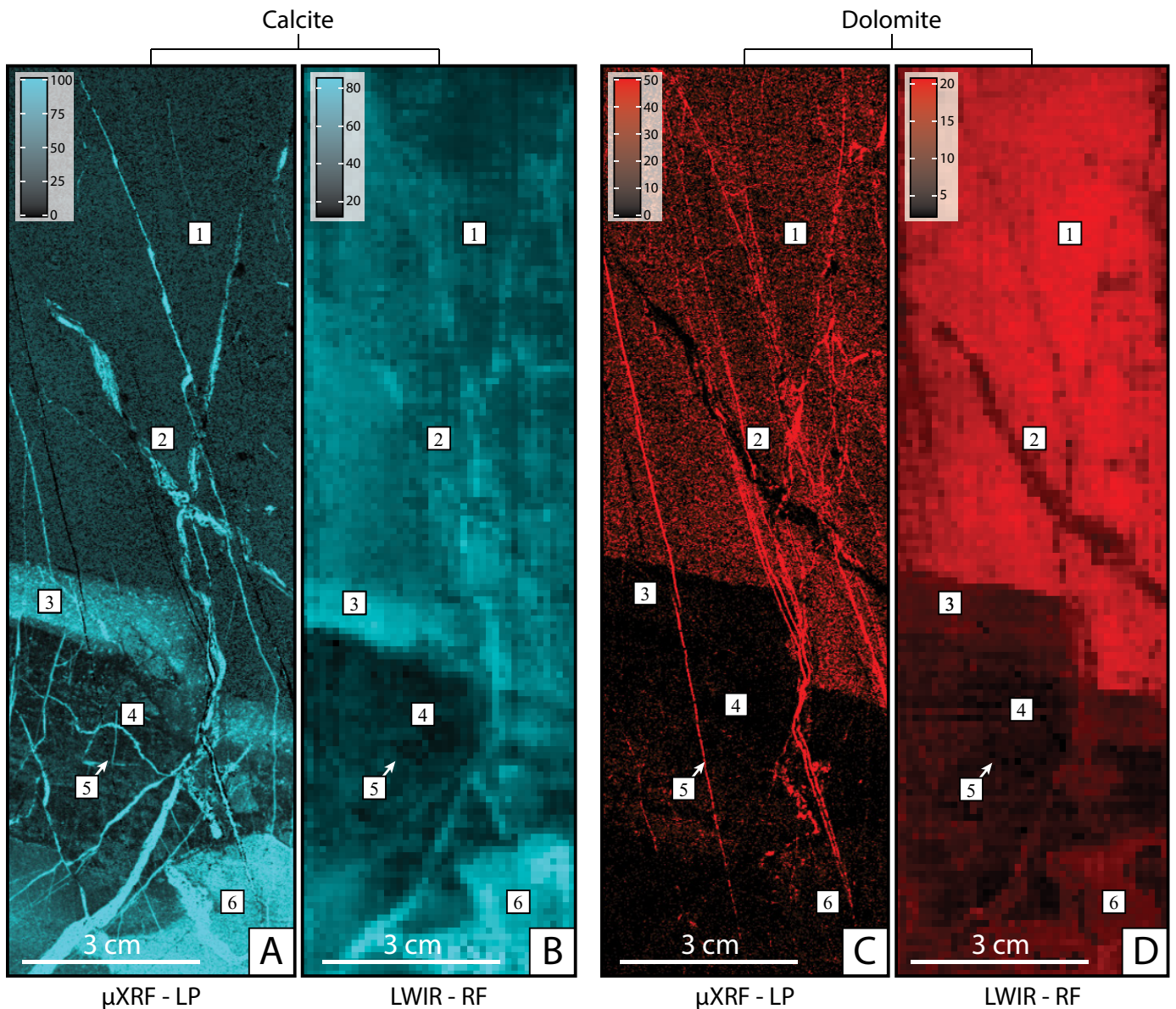
Fig. 7. Quantified μXRF-derived mineralogy maps compared to Random Forest-derived LWIR mineralogy maps for calcite (A) and (B) and dolomite (C) and (D) of sample M180080. Sections of the sample are numbered based on textural differences. (1) = relatively unaltered host rock, (2) = calcite + quartz veins in the unaltered host rock, (3) = silicification front, (4) = zone of pervasive silicification, (5) = thin dolomite vein, and (6) = zone of high calcite in the lower right corner of the image.

cases, the important variable may be a lack of characteristic feature or the approach to a peak (i.e., a peak shoulder).

Regression model results compared to multielement geochemistry

The Random Forest mineral models were run on LWIR images of 2,030 m of drill core from seven drill holes. The mineralogy results were converted to chemistry and aggregated to multielement geochemistry data intervals at 5, 10, and 20 ft for external validation of Random Forest model results (Fig. 10). Multielement proportions for Al, Ca, K, and Mg are measured via 4-acid digest method and C and Si were estimated from the 4-acid digest data (see "Methods") because neither C nor Si are measured in the 4-acid digest analysis. The calculated Si and C was compared to the measured values for Si and C (geochemistry results from this study using whole-rock XRF for Si and LECO analyses for total C) for validation of this Si and C estimation method (Fig. 11), which produced results with absolute error of ±4.5% for CO_2 and ±4.1% for SiO_2. The comparison produced RMSE values of 1.06 (Al), 4.55 (Ca), 1.65 (K), and 2.19 (Mg) when compared to measured values. Compared to calculated concentrations, RMSE values were 1.24 (C) and 6.19 (Si). Elements Al, C, Ca, and Si have regression lines with slopes close to one, intercepts near zero, and R^2 values that range from 0.55 (Mg) to 0.94 (C and Ca). Potassium and magnesium appear to be slightly overestimated by the models overall and both have a lower R^2 value.
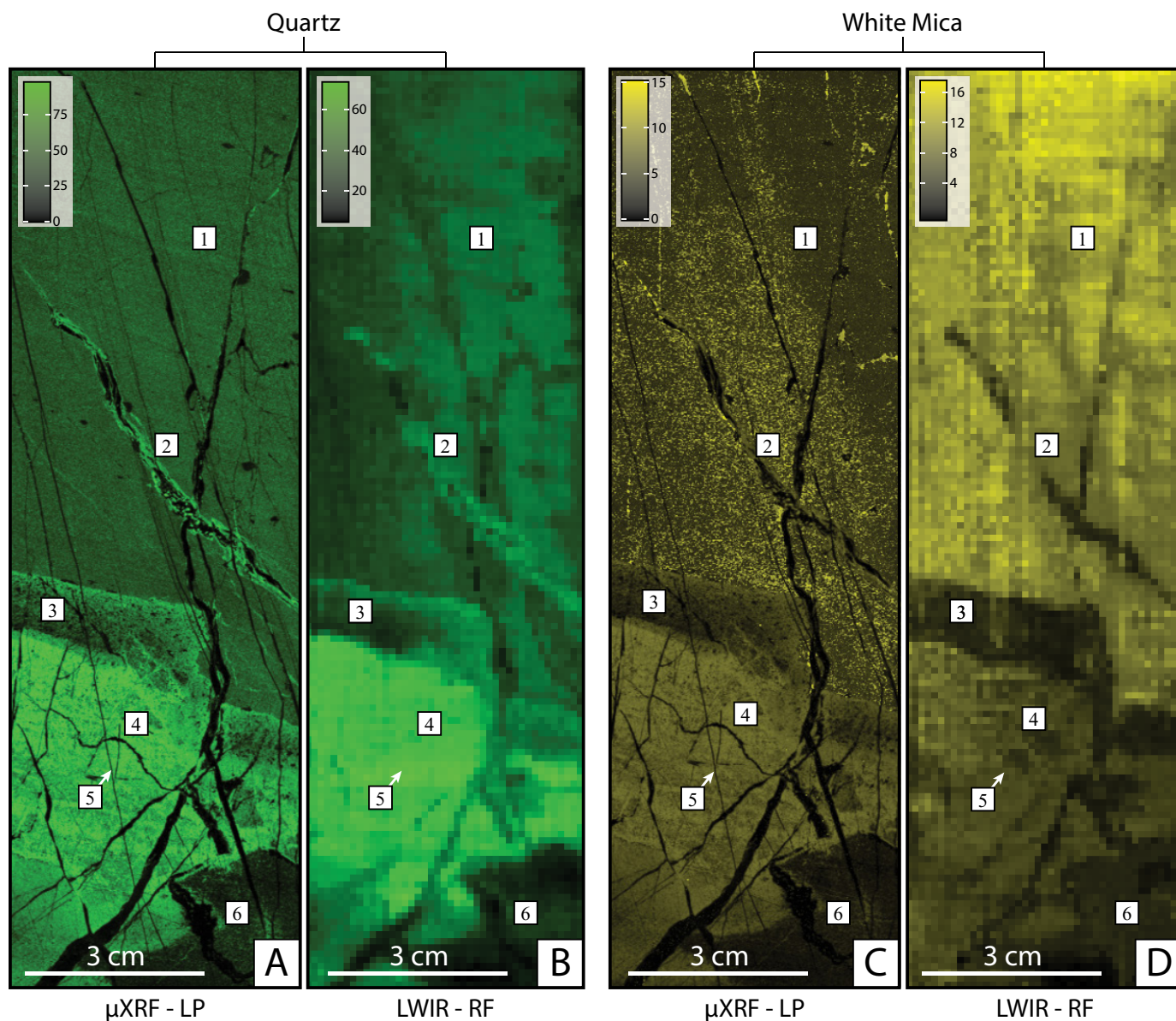
Fig. 8. Quantified *μ*XRF-derived mineralogy maps compared to Random Forest-derived LWIR mineralogy maps for quartz (A) and (B) and white mica (C) and (D) of sample M180080. Sections of the sample are numbered based on textural differences. (1) = relatively unaltered host rock, (2) = calcite + quartz veins in the unaltered host rock, (3) = silicification front, (4) = zone of pervasive silicification, (5) = thin dolomite vein, and (6) = zone of high calcite in the lower right corner of the image.

Discussion

LWIR regression models

Feely and Christensen (1999) used a linear spectral deconvolution algorithm to quantify mineral mixtures for major rock-forming minerals using LWIR. They reported residual errors of ±7 to 15% for minerals such as feldspar, quartz, calcite and dolomite, as compared to our Random Forest predictive RMSE of 1.17 to 6.75% and external RMSE of 1.06 to 6.19% (compared to QXRD) for calcite, dolomite, kaolinite, white mica, K-feldpsar, phlogopite, and quartz derived using our modeled Random Forest regression.

Whereas the error of each method is comparable, the methods for mineral identification are very different. The spectral unmixing method requires a complete library of characteristic spectra that represent the minerals present within the samples. Feely and Christensen (1999) also reported on results from coarse-grained rocks, whereas the samples from this study contain very fine-grained minerals. The utility of linear deconvolution is limited in fine-grained rocks due to additional spectral features caused by volume scattering, which is difficult to account for in spectral libraries (Hubbard et al., 2018). The benefit of linear spectral deconvolution is that an accurately defined spectral library can be transferable to other field areas without additional data (as long as the samples have sufficiently coarse grain sizes). However, an incomplete library, or a library that contains characteristic spectra of minerals not present in the system, can lead to large increases in error or
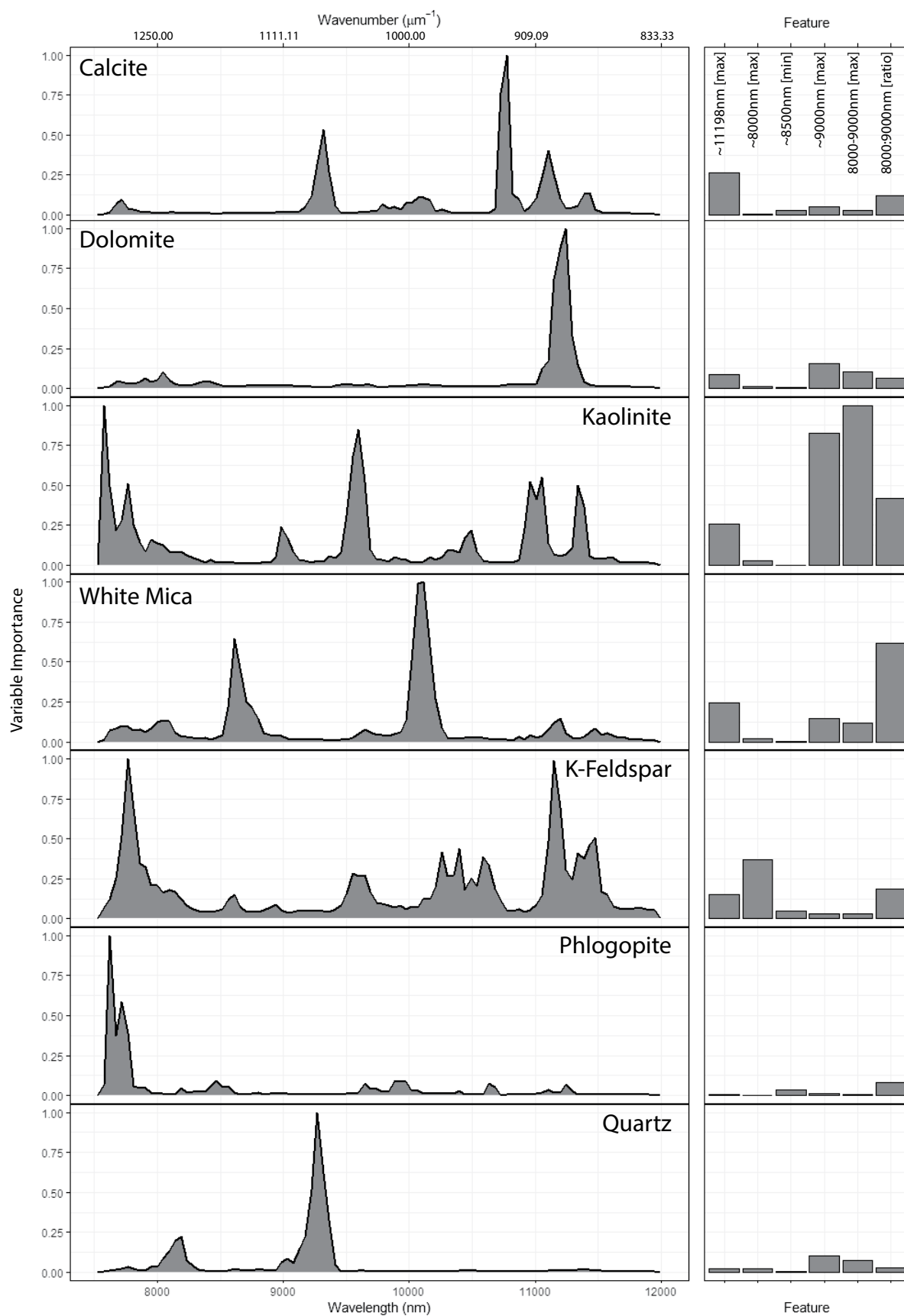
Fig. 9. Variable importance (scaled) as a function of wavelength and spectral feature for each Random Forest mineral model.
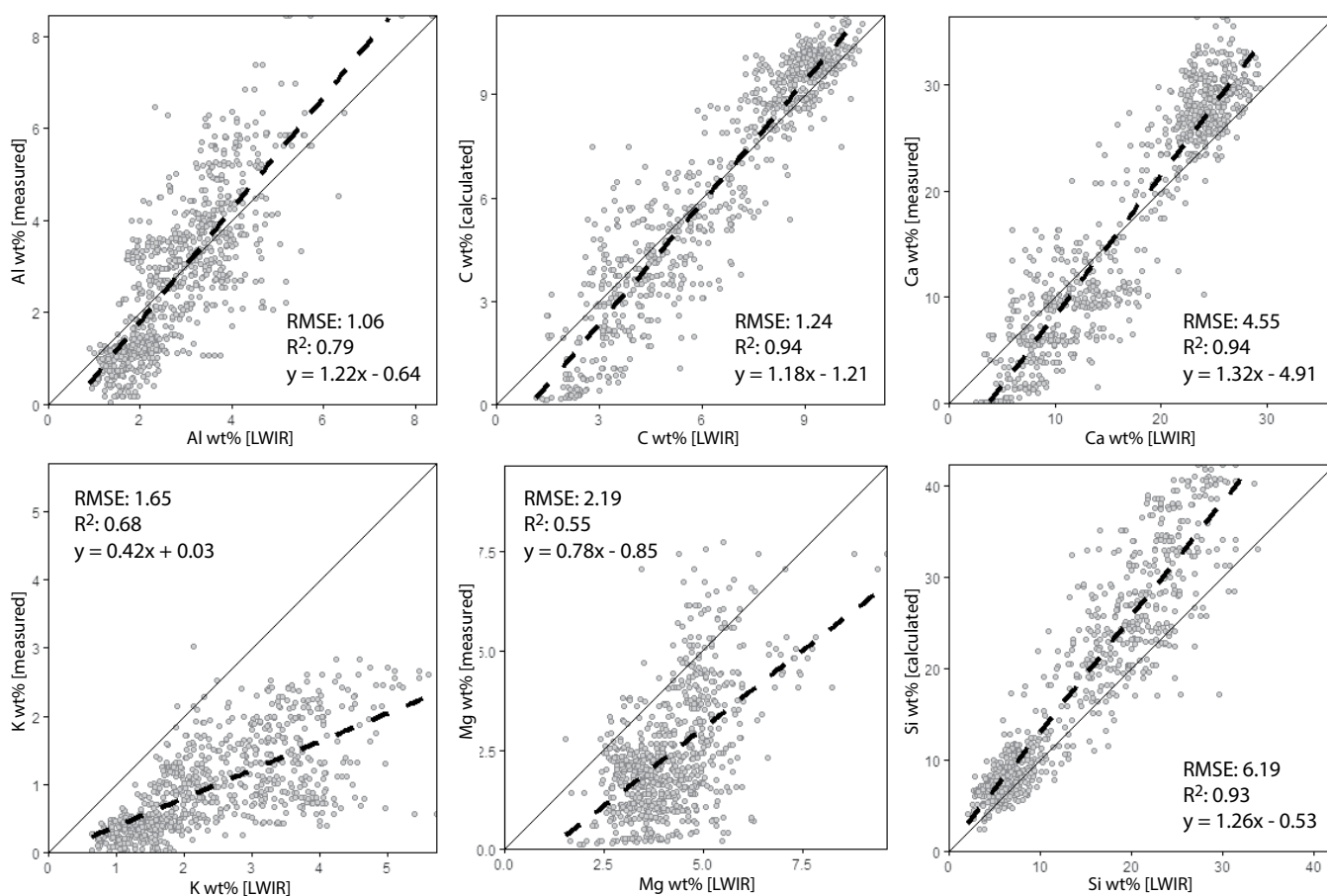
Fig. 10. Multielement geochemistry (Al, Ca, K, and Mg) and calculated chemistry from multielement measurements (C and Si) compared to chemistry calculated from Random Forest results at the same intervals from the 2,030 m of LWIR-scanned drill core. RMSE, R2, and regression line equation shown as insets for each element. Dark dashed line represents regression line and thin black line is 1/1.

compensation by misidentification of a combination of other minerals (Rogge et al., 2006; Hecker et al., 2012). In contrast, the Random Forest regression modeling approach presented here does not require a spectral library to be produced for each individual geologic domain. Furthermore, the approach adopted in this study provides a built-in baseline (whereby other analytical results are used for training data), with error measurement to evaluate the robustness of the results.

The visual comparison of calcite, quartz, and dolomite μXRF-derived mineralogy (Figs. 7A, C, 8A, C, using the methods presented in Barker et al., 2020) and the results of the LWIR regression model (LWIR interpreted mineralogy) on a test sample (M180080), which was omitted from the training data (see Figs. 7, 8), show that the two produce a similar geometric distribution of mineralogy. Figure 7B has textural and mineralogical results consistent with a carbonate host rock that has been decalcified and later crosscut by calcite veins. The resulting image is interpreted to represent a decalcification front with the image top being relatively unaltered and the bottom almost completely decalcified in some areas. Figure 8B shows the silica replacement that often occurs during, or after, decalcification of carbonate rocks in Carlin-type systems (Cline et al., 2005). It also shows quartz veins and the distribution of primary quartz in the unaltered silty carbonate.

Due to the difference in spatial resolution (100 μm μXRF and 1.2 mm for LWIR), much of the finer scale details have been lost in the LWIR images. Veins with a width of <1 mm are not identifiable in the Random Forest-predicted LWIR images. There are also small discrepancies (error) between the two image types, especially in the fine-grained host rock. Two of the LWIR images (calcite and quartz) show what may be a "shadow" effect (Figs. 7B, 8B). This may be due to a slightly uneven heating of the sample during analysis. Visually, the LWIR-predicted mineralogy images are comparable to the μXRF-derived mineralogy map with similar mineral abundances and provide details that are beneficial in understanding the alteration that has occurred in this sample.

A final external validation showed that the Random Forest regression models produced results comparable to multielement geochemistry over the scanned 2,030 m of drill core (at 5-, 10-, and 20-ft intervals). The relatively low RMSE (1.06–6.19%) suggest that despite the difference in data type, scale, and source (surface scans versus whole-rock analyses from split core from the same intervals), the Random Forest models produced mineral abundance estimates with chemical components that are consistent with the multielement geochemistry. The low R^2 value and shallow slope of the regression line for K and Mg suggests that these elements have been
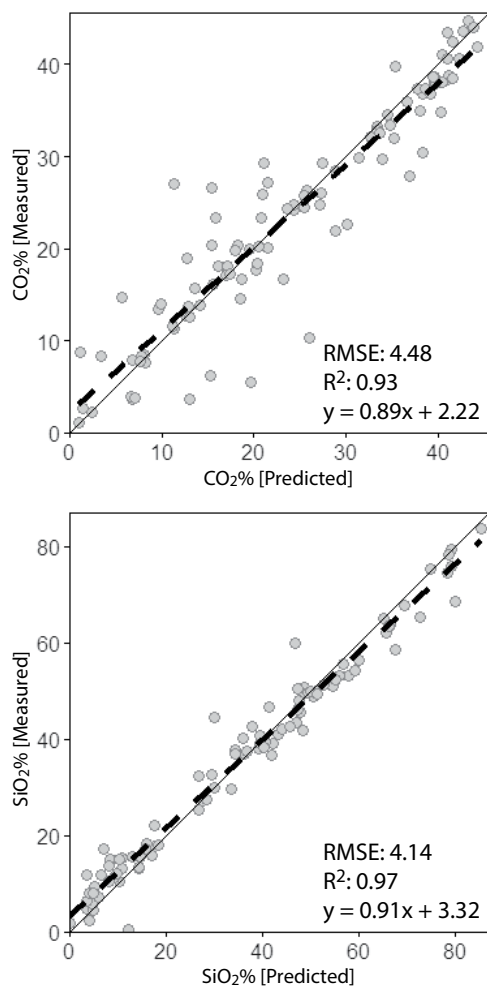
of this method is in the turnaround time. This method can be completed in-house by workers with an understanding of the particular geologic system in question by collecting samples containing representative mineralogy and creating a training dataset using commercially available analytical rastering technique such as μXRF (as described in Barker, et. al., 2020) or quantitative SEM (e.g. MLA, QEMSCAN; Gottlieb, 2008). Being able to describe the mineralogical variations quantitively and with more confidence, potentially in "real time" as core scanning proceeds, may lead to the discovery of new exploration vectors for Carlin-type and other mineralization styles, particularly in fine-grained sedimentary rocks. Use of this method can provide detailed logs of mineralogy that can be used by geologists to better understand paragenesis and alteration. It may also provide value to metallurgists who can understand the relative abundance of quartz, carbonate, and clay mineralogy, which could affect hardness and mineral processing characteristics (Escolme et al., 2019).

Conclusion

In this study LWIR was used to predict mineral abundances using Random Forest regression models. Results of the Random Forest regression models indicate that the use of μXRF-derived mineralogy to inform LWIR of mineral proportions using Random Forest modeling can produce relatively accurate and precise mineral estimates. The RMSE rates from this study (1.17–6.75% internal and 1.06–6.19% external) are comparable to error of proportion estimates of a linear spectral deconvolution algorithm ($\pm$7–15%), a commonly used spectral unmixing method.

Acknowledgments

Fig. 11. Validation of CO_2 and SiO_2 prediction from measured whole-rock XRF for Si and LECO analyses for C_{total} from this study. CO_2 predicted by calculating total carbonate and SiO_2 predicted by assuming missing mass is silica. Predicted values compared to measured values from whole-rock chemical analyses. Regression line and 1/1 line shown as dashed and thin black lines, respectively.

overestimated by the Random Forest models. The difficulty of distinguishing white mica from K-feldspar and phlogopite in the μXRF training data likely contributes to error in the K, whereas the high detection limit of Mg in the μXRF method may have contributed to error in identifying Mg-bearing minerals. However, the results of Al, C, and Ca suggest that the total aluminosilicate and carbonate mineral predictions are accurate. With the development of a more sensitive μXRF analyzers such as the Bruker Tornado Plus (Bruker, 2018b), with lower detection limits for the light elements, Mg predictions may be improved.

The strength of the Random Forest regression models is in their ability to estimate (with relative accuracy and precision) the mineral proportions of complicated spectral mixtures in fine-grained mineralogical systems such as Carlin-type gold deposits. This method is especially useful for data-rich projects, such as those typically managed by the mining industry. Such projects often have multiple datasets readily available that can be used for training LWIR spectra. An additional advantage

REFERENCES

Ahmed, A.D., 2010, Beyond the confines of the ore deposit: Mapping low temperature hydrothermal alteration above, within, and beneath Carlin-type gold deposits: M.S. thesis, Vancouver, University of British Columbia, 197 p.

Ahmed, A.D., Hickey, K.A., and Barker, S.L.L., 2009, Tracing the distal hanging wall expression of Carlin-type hydrothermal fluids: A possible road-map to subsurface Au-deposits, in thermal and geochemical footprints of low-temperature sedimentary rock-hosted hydrothermal Au-systems: Identifying far-field vectors toward ore: Year 2 Technical Summary, Mineral Deposit Research Unit, University of British Columbia, p. 4.1–4.18.

Arne, D., House, E., Pontual, S., and Huntington, J., 2016, Hyperspectral interpretation of selected drill cores from orogenic gold deposits in central Victoria, Australia: Australian Journal of Earth Sciences, v. 63, p. 1003–1025.

Bakken, B.M., 1990, Gold mineralization, wall-rock alteration and the geochemical evolution of the hydrothermal system in the main ore body, Carlin mine, Nevada: Ph.D. dissertation, Stanford, California, Stanford University, 256 p.

Barker, R.D., 2017, Geochemical and mineralogical investigation of breccias at the El Niño Au-Ag deposit, Elko County, Nevada: M.S. thesis, Fort Collins, Colorado, Colorado State University, 221 p.

Barker, R.D., and Ridley, J., 2020, Mineralization, alteration, and breccias of the El Niño Au-Ag deposit, Elko County, Nevada, 2020, in Koutz, F.R., and

Pennell, W.M., eds., Vision for discovery, geology and ore deposits of the Basin and Range: Geological Society of Nevada Symposium Volume, Reno, Nevada, 2020, p. 311–338.

Barker, R.D., Barker, S.L.L., Wilson, S.A., and Stock, E.D., 2020, Quantitative mineral mapping of drill core surfaces I: A method for μXRF mineral calculation and mapping of hydrothermally altered, fine-grained sedimentary rocks from a Carlin-type gold deposit: Economic Geology, v. 116, p. 000.

Barrick Gold Exploration Inc., 2019, Q1 Report: Internal Quarterly Report, 93 p.

Barthelme, S., 2018, Imager: Image processing library based on "CImg," R package version 0.41.1.

Bedell, R.L., and Coolbaugh, M.F., 2009, Appendix 2: Atmospheric corrections: Reviews in Economic Geology, v. 16, p. 257–263.

Bedell, R.L., Rivard, B., Browning, D., and Coolbaugh, M.F., 2017, Thermal infrared sensing for exploration and mining—an update on relevant systems for remote acquisition to drill core scanning: Exploration 17, Sixth Decennial International Conference on Mineral Exploration 2017, Proceedings, p. 881–897.

Bradford, M.S., 2008, Mapping clay alteration across the northern Goldstrike property using spectroscopy and remote sensing, Eureka County, Nevada: M.S. thesis, Bowling Green, Ohio, Bowling Green State University, 81 p.

Breiman, L., 2001, Random Forests: Machine Learning, v. 45, no.1, p. 5–32.

Breiman, L., Friedman, J.H., Olshen, R.A., and Stone, C.J., 1984, Classification and regression trees: Boca Raton, FL, Chapman and Hall/CRC, 358 p.

Browning, D., 2014, Hyperspectral remote sensing in mineral exploration: Ammonium-illite as a pathfinder for gold: M.S. thesis, Moscow, Idaho, University of Idaho, 102 p.

Brownlee, J., 2018, Master machine learning algorithms: Discover how they work and implement them from scratch: Melbourne, Machine Learning Mastery, v. 1.13, 153 p.

Bruker, 2018a, ESPRIT 2: Software for micro- and nano-analysis, (https://www.bruker.com/products/x-ray-diffraction-and-elemental-analysis/eds-wds-ebsd-sem-micro-xrf-and-sem-micro-ct/esprit-2.html).

——2018b, M4 Tornado Plus: Super light element micro-XRF spectrometer. (https://www.bruker.com/products/x-ray-diffraction-and-elemental-analysis/micro-xrf-and-txrf/m4–tornado-plus/overview.html).

——2018c, M4 Tornado: 2D Micro-XRF with ultimate speed and accuracy, (https://www.bruker.com/products/x-ray-diffraction-and-elemental-analysis/micro-xrf-and-txrf/m4–tornado/overview.html).

Canty, M.J., 2014, Image analysis, classification and change detection in remote sensing: with algorithms for ENVI/IDL and Python: Boca Raton, Florida, CRC Press, 3rd ed., 541 p.

Clark, R.N., and Roush, T.L., 1984, Reflectance spectroscopy: Quantitative analysis techniques for remote sensing applications: Journal of Geophysical Research: Solid Earth, v. 89, no. B7, p. 6329–6340.

Clark Maroun, L.R., Cline, J.S., Simon, A., Anderson, P., and Muntean, J., 2017, High-grade gold deposition and collapse breccia formation, Cortez Hills Carlin-type gold deposit, Nevada, USA: Economic Geology, v. 112, p. 707–740.

Cline, J.S., Hofstra, A.H., Muntean, J.L., Tosdal, R.M., and Hickey, K.A., 2005, Carlin-type gold deposits in Nevada: Critical geologic characteristics and viable models: Economic Geology 100th Anniversary Volume, p. 451–484.

Crósta, A.P., De Souza Filho, C.R., Azevedo, F., and Brodie, C., 2003, Targeting key alteration minerals in epithermal deposits in Patagonia, Argentina, using ASTER imagery and principal component analysis: International Journal of Remote Sensing, v. 24, no.21, p. 4233–4240.

Emsbo, P., Hofstra, A.H., Lauha, E.A., Griffin, G.L., and Hutchinson, R.W., 2003, Origin of high-grade gold ore, source of ore fluid components, and genesis of the Meikle and neighboring Carlin-type deposits, northern Carlin Trend, Nevada: Economic Geology, v. 98, p. 1069–1105.

Escolme, A., Berry, R.F., Hunt, J., Halley, S., and Potma, W., 2019, Predictive models of mineralogy from whole-rock assay data: Case study from the Productora Cu-Au-Mo deposit, Chile: Economic Geology, v. 114, p. 1513–1542.

Feely, K.C., and Christensen, P.R., 1999, Quantitative compositional analysis using thermal emission spectroscopy: Application to igneous and metamorphic rocks: Journal of Geophysical Research: Planets, v. 104, p. 24195–24210.

Flude, S., Haschke, M., and Storey, M., 2017, Application of benchtop micro-XRF to geological materials: Mineralogical Magazine, v. 81, p. 923–948.

Gillespie, A.R., 1992, Spectral mixture analysis of multispectral thermal infrared images: Remote Sensing of Environment, v. 42, p. 137–145.

Gottlieb, P., 2008, The revolutionary impact of automated mineralogy on mining and mineral processing: International Mineral Processing Congress, 24th, Beijing, China, September 2008, Proceedings, p. 165–174.

Han, J., Chu, G., Chen, H., Hollings, P., Sun, S., and Chen, M., 2018, Hydrothermal alteration and short wavelength infrared (SWIR) characteristics of the Tongshankou porphyry-skarn Cu-Mo deposit, Yangtze craton, eastern China: Ore Geology Reviews, v. 101, p. 143–164.

Hecker, C., Dilles, J.H., van der Meijde, M., and van der Meer, F.D., 2012, Thermal infrared spectroscopy and partial least squares regression to determine mineral modes of granitoid rocks: Geochemistry, Geophysics, Geosystems–G3, v. 13, no. 3, p. 1–15.

Hijmans, R.J., 2018, Raster: Geographic Data Analysis and Modeling. R package version 2.8–4.

Hooper, B., Stephen, D., and Peacock, M., 2018, Pathfinder exploration techniques targeting porphyry and epithermal alteration systems in the Temora copper-gold belt [ext. abs.]: Australian Society of Exploration Geophysicists, ASEG Extended Abstracts, v. 2018, no. 1, p. 1–8.

Hubbard, B. E., Hooper, D. M., Solano, F., and Mars, J. C., 2018, Determining mineralogical variations of aeolian deposits using thermal infrared emissivity and linear deconvolution methods: Aeolian Research, v. 30, p. 54–96.

Jin, X., 2017, ENVI automated image registration solutions: Harris Corporation, Internal Report, 26 p.

Kuhn, M., 2020, Caret: Classification and regression training. R package version 6.0–85.

Lane, M.D., and Christensen, P.R., 1997, Thermal infrared emission spectroscopy of anhydrous carbonates: Journal of Geophysical Research: Planets, v. 102, p. 25581–25592.

Laukamp, C., Lau, I., Stolf, M., and Green, A., 2018, Influence of quartz grain size on the quantification of kaolinite using infrared reflectance spectroscopy: International Mineralogical Association Meeting, 22nd, Melbourne, Australia, August 2018, Proceedings, p. 96

Liaw, A., and Wiener, M., 2002, Classification and regression by random Forest: R News, v. 2, no. 3, p. 18–22.

Mateer, M.A., 2010, Ammonium illite at the Jerritt Canyon district and Goldstrike property, Nevada: Its spatial distribution and significance in the exploration of Carlin-type deposits: Ph.D. dissertation, Laramie, WY, University of Wyoming, 214 p.

Mauger, A.J., Gordon, G.A., Reid, A., and Kitto, J., 2012, Quantifying downhole silicate mineralogy-HyLogger with thermal infrared [ext. abs.]: Australian Society of Exploration Geophysicists, ASEG Extended Abstracts, v. 2012, no. 1, p. 5.

Maydagán, L., Franchini, M., Impiccini, A., and Lentz, D., 2016, Phyllosilicates geochemistry and distribution in the Altar porphyry Cu-(Au) deposit, Andes Cordillera of San Juan, Argentina: Applications in exploration, geothermometry, and geometallurgy: Journal of Geochemical Exploration, v. 167, p. 83–109.

McDowell, M., Hamilton, V., Cady, S., and Knauth, P., 2009, Thermal infrared and visible to near-infrared spectral analysis of chert and amorphous silica, *in* McDowell, M., ed., Lunar and Planetary Science Conference, 40th, Proceedings, v. 40, p. 2.

Nash, D.B., and Salisbury, J.W., 1991, Infrared reflectance spectra (2.2–15 μm) of plagioclase feldspars: Geophysical Research Letters, v. 18, p. 1151–1154.

Neal, L.C., Wilkinson, J.J., Mason, P.J., and Chang, Z., 2018, Spectral characteristics of propylitic alteration minerals as a vectoring tool for porphyry copper deposits: Journal of Geochemical Exploration, v. 184, p. 179–198.

Pour, A.B., and Hashim, M., 2015, Hydrothermal alteration mapping from Landsat-8 data, Sar Cheshmeh copper mining district, south-eastern Islamic Republic of Iran: Journal of Taibah University for Science, v. 9, no. 2, p. 155–166.

Quinlan, J.R., 1986, Induction of decision trees: Machine Learning, v. 1, no. 1, p. 81–106.

R Core Team, 2017, R: A language and environment for statistical computing: Vienna, Austria, R Foundation for Statistical Computing, v. 3.5.2.

Ramsey, M.S., 2004, Quantitative geological surface processes extracted from infrared spectroscopy and remote sensing, *in* Molecules to Planets: Infrared Spectroscopy in Geochemistry, Exploration Geochemistry and Remote Sensing: Mineralogical Association of Canada, v. 33, Chapter 8, 17 p.

Ramsey, M.S., and Christensen, P.R., 1998, Mineral abundance determination: Quantitative deconvolution of thermal emission spectra: Journal of Geophysical Research: Solid Earth, v. 103, p. 577–596.

Rogge, D.M., Rivard, B., Jinkai, Z., and Jilu, F., 2006, Iterative spectral unmixing for optimizing per-pixel endmember sets: IEEE Transactions on Geoscience and Remote Sensing, v. 44, p. 3725–3736.

Salisbury, J.W., 2020, John Hopkins University spectral library, https://speclib.jpl.nasa.gov/library.

Smith, G.M., and Milton, E.J., 1999, The use of the empirical line method to calibrate remotely sensed data to reflectance: International Journal of Remote Sensing, v. 20, p. 2653–2662.

Smith, R.J., 2009, Use and misuse of the reduced major axis for line-fitting: American Journal of Physical Anthropology, v. 140, p. 476–486.

Tappert, M.C., Rivard, B., Tappert, R., and Feng, J., 2013, Using reflectance spectroscopy to estimate the orientation of quartz crystals in rocks: Canadian Mineralogist, v. 51, p. 405–413.

Tappert, M.C., Rivard, B., Fulop, A., Rogge, D., Feng, J., Tappert, R., and Stalder, R., 2015, Characterizing kimberlite dilution by crustal rocks at the Snap Lake diamond mine (Northwest Territories, Canada) using SWIR (1.90–2.36 μm) and LWIR (8.1–11.1 μm) hyperspectral imagery collected from drill core: Economic Geology, v. 110, p. 1375–1387.

Teal, L., and Jackson, M., 2002, Geologic overview of the Carlin Trend gold deposits: Gold deposits of the Carlin Trend: Nevada Bureau of Mines and Geology Bulletin, v. 111, p. 9–19.

Vaughan, J.R., Hickey, K.A., and Barker, S.L.L., 2016, Isotopic, chemical, and textural evidence for pervasive calcite dissolution and precipitation accompanying hydrothermal fluid flow in low-temperature, carbonate-hosted, gold systems: Economic Geology, v. 111, p. 1127–1157.

Wells, J.D., and Mullens, T.E., 1973, Gold-bearing arsenian pyrite determined by microprobe analysis, Cortez and Carlin gold mines, Nevada: Economic Geology, v. 68, p. 187–201.

Wells, J.D., Stoiser, L.R., and Elliott, J.E., 1969, Geology and geochemistry of the Cortez gold deposit, Nevada: Economic Geology, v. 64, p. 526–537.

Yitagesu, F.A., van Der Meer, F., van Der Werff, H., and Hecker, C., 2011, Spectral characteristics of clay minerals in the 2.5–14 μm wavelength region: Applied Clay Science, v. 53, p. 581–591.

Zaini, N., Meer, F., and van der Werff, H., 2012, Effect of grain size and mineral mixing on carbonate absorption features in the SWIR and TIR wavelength regions: Remote Sensing, v. 4, p. 987–1003.

Rocky Barker obtained his M.Sc. degree in geoscience from Colorado State University in 2017. He has worked as a geoscientist and data science consultant in the mineral industry for companies such as Barrick Gold Exploration Inc., Nevada Gold Mines, and AusSpec. He is currently a third-year Ph.D. candidate at the University of Waikato in Hamilton, New Zealand. Rocky's Ph.D. work focuses on the prediction of mineralogy and mineral chemistry in a Carlin-type gold deposit using hyperspectral infrared data. His study involves the integration of geochemical datasets collected at various scales, supported by machine learning methods.